Exploring optical properties of $La_2Hf_2O_7:Pr^{3+}$ nanoparticles under UV and X-ray excitations for potential lighting and scintillating applications

Journal:	*New Journal of Chemistry*
Manuscript ID	NJ-ART-02-2018-000895.R1
Article Type:	Paper
Date Submitted by the Author:	28-Mar-2018
Complete List of Authors:	Zuniga, Jose; The University of Texas Rio Grande Valley Gupta, Santosh; BARC, Pokhrel, Madhab; University of Texas Rio Grande Valley College of Sciences, Chemistry Mao, Yuanbing; University of Texas - Pan American, Department of Chemistry

Exploring optical properties of $La_2Hf_2O_7:Pr^{3+}$ nanoparticles under UV and X-ray excitations for potential lighting and scintillating applications

Jose Zuniga[1], Santosh K. Gupta[1,2], Madhab Pokhrel[1,3], Yuanbing Mao[1,4*]

[1]Department of Chemistry, University of Texas Rio Grande Valley, 1201 West University Drive, Edinburg, Texas 78539, USA

[2]Radiochemistry Division, Bhabha Atomic Research Center, Mumbai, India, 400085

[3]Department of Physics, University of Texas Rio Grande Valley, 1201 West University Drive, Edinburg, Texas 78539, USA

[4]School of Earth, Environmental, and Marine Sciences, University of Texas Rio Grande Valley, 1201 West University Drive, Edinburg, Texas 78539, USA

[*]To whom correspondence should be addressed. Email: yuanbing.mao@utrgv.edu, Tel.: +1-956-665-2986.

Abstract:

New optical materials with efficient luminescent and scintillating properties have drawn great attention due to the demand for optoelectronic devices and medical theronostics. Their nanomaterials are expected to reduce cost while incrementing efficiency for potential lighting and scintillator applications. In this study, we have developed praseodymium doped lanthanum hafnate ($La_2Hf_2O_7:Pr^{3+}$) pyrochlore nanoparticles (NPs) using a combined co-precipitation and relative low temperature molten salt synthesis procedure. XRD and Raman investigations confirmed ordered pyrochlores phase for the as-synthesized undoped and Pr^{3+} doped $La_2Hf_2O_7$ NPs. Emission profile displayed the involvement of both $^3P_0$ and $^1D_2$ states in the photoluminescence process, however the intensity of emission from $^1D_2$ states was found to be higher than that from $^3P_0$ states. This can have huge implication in designing novel red phosphor for possible application in solid-state lighting. As a function of Pr^{3+} concentration, we found that the 0.1% Pr^{3+} doped $La_2Hf_2O_7$ NPs possess the strongest emission intensity with a quantum yield of 20.54 ± 0.1%. Concentration quenching in this case is mainly induced by cross-relaxation process $^3P_0 + {}^3H_4 \rightarrow {}^1D_2 + {}^3H_6$. Emission kinetics studies shows that fast decaying species arises because of Pr^{3+} ions occupying Hf^{4+} site whereas slow decaying species can be attributed to Pr^{3+} ions occupying La^{3+} site of the pyrochlore structure of $La_2Hf_2O_7$. X-ray excited luminescence (XEL) showed strong red-light emission, manifesting that the material is a promising scintillator for radiation detection. In addition, photon counts were found to be much higher when NPs is exposed to X-ray compared to ultraviolet light. Altogether, these $La_2Hf_2O_7:Pr^{3+}$ NPs have the potential to be a good down conversion phosphor as well as scintillator material.

1. Introduction

Apart from numerous applications in various advanced fields such as light emitting diodes,[1] laser,[2] biomedical,[3] catalysis,[4] and solar cells,[5] lanthanide ion doped phosphor materials can also be used as scintillators or dosimeters depending upon the applications and processes involved.[6] Scintillation materials are also used for various applications ranging from photodynamic therapy,[7] security,[8] well-logging,[9] medical imaging,[10] etc. Research based on exploring novel scintillator materials is one field that is getting intense attention in last ten years and the lookout for rapid and efficient materials for such applications is always going to be the main research area in this particular field. The process of scintillation is a type of radioluminescence (RL) in which high-energy photons are absorbed and finally lead to an emission of light. It typically consists of three different steps: (i) incoming radiation is converted into a large number of electron−hole (e^--h^+) pairs, (ii) energy transfer from e^--h^+ pairs to luminescent active ions, and (iii) radiative emission due to de-excitation of luminophors from an excited state to the ground state. Scintillators are usually considered best if it possesses various favorable properties such as high density, effective Z-number, emission output, energy resolution, and radiation hardness in addition to being easy to grow in large quantity at low cost.[11]

The system having $Ln_2M_2O_7$ compositions (Ln: trivalent lanthanides, M: tetravalent titanium group elements, such as Ti, Zr and Hf) has been explored extensively because of their various scientific and technological importance in various areas such as gas sensors,[12] thermal barrier coatings,[13] solid oxide fuel cells,[14] neutron absorbing materials,[15] nuclear waste hosts,[16] etc. Structure plays a very crucial role for all applications mentioned above. These compounds are known to exist in two structural variants, ordered pyrochlore and disordered fluorite structures, each having specific applications. A cubic pyrochlore structure is preferred and is more suited for scintillator materials because the oxygen vacancies are well distributed through the lattice of the hosts giving a sense of symmetry to the overall structure and therefore sintering them into transparent ceramic would be easier.[17] On the other hand, cubic defect fluorite structure has a random distribution of the oxygen vacancies in the structure, which is not suitable for scintillators.[18] The phase transition can be induced chemically by doping or applying higher temperature and pressure. The phase transformation from ordered pyrochlore to defect fluorite involves the randomization of the oxygen ions among the 48f, 8b, and 8a sites, and the cations between the 16c and 16d sites .[19] Among various pyrochlores, $La_2Hf_2O_7$, lanthanum hafnate,

stands out as a material with special properties for optical applications. $La_2Hf_2O_7$ offers a set of properties that makes it very attractive for novel high-energy radiation detectors. These properties include high stopping power for X- and γ-rays with $Z_{Hf} = 72$ and high density of 7.9 g/cm^3.[17, 18] Despite of various favorable properties, hafnate pyrochlores have not been given due credit compared to their titanate and zirconate counterparts. Our group[19] have investigated the photoluminescence (PL) and RL properties of $La_2Hf_2O_7:Eu^{3+}$ whereas Hansel *et al*[20] have explored the same material for non-contact thermometry. We have also carried out systematic studies on structural and optical properties of various Eu^{3+}-doped rare earth (RE) hafnates $RE_2Hf_2O_7$ (RE = Y, La, Pr, Gd, Er, and Lu) nanoparticles (NPs).[21] The interest in the Pr^{3+} intra-configurational (f-f) and inter-configurational (f-d) emission arises from their possible potential applications in solid state lighting, display devices, medical and security industries.[22] Host such as $La_2Hf_2O_7$ is expected to yield good radioluminescence on doping with Pr^{3+} due to its favorable properties mentioned above, specifically high stopping power for X-ray and γ-rays and high density. As far as dopant ion is concerned, hence we wanted to check the materials characteristics and optical and scintillation properties of trivalent praseodymium ion doped $La_2Hf_2O_7$.

Furthermore, Pr^{3+} is a unique lanthanide ion as it emits in visible as well as near infrared regions of the electromagnetic spectrum. It is frequently used as an optical component for solid state based lighting in view of its ability to exhibit up-conversion process, wherein blue light is emitted from $^3P_0$ level upon multiple photon pumping of the $^1G_4$ or $^1D_2$ levels.[23] There are few works on exploring $La_2Hf_2O_7$ for scintillator application with dopant such as Cerium (III)[24] and Titanium (IV)[25]. It is also unique in a way that both trivalent as well as tetravalent dopant can be localized at Ln^{3+}- and M^{4+}-sites of the $Ln_2M_2O_7$ compositions, respectively. Trojan-Piegza and the group have explored the PL and RL properties of $La_2Hf_2O_7:Pr^{3+}$ NPs synthesized by a Pechini sol-gel method.[18, 26] In one case, they recorded the PL and RL of their NPs after annealed at 1000 and 1400^{o}C.[18, 26] In another case, they compared the PL and RL properties of powder and ceramic forms.[18, 26] Structural analysis in these papers were probed using X-ray diffraction (XRD) only. X-ray is scattered by electrons, so high atomic number elements including Ln and Hf are stronger scatterer of X-ray compared to oxygen atoms. Therefore, X-ray fails to give information pertaining to oxygen ions. This information is very important if one needs to explore pyrochlore based materials for various optical, electrical and other technological applications.

Sometimes, it is even very difficult to distinguish completely disordered pyrochlore phase from a fluorite compound by XRD. Considering the reconstructive nature at the transition of these two phases, there may also be chances that these two phases co-exist sometimes. In this sense, other techniques such as Raman and Fourier-transform infrared (FTIR) spectroscopies are advantageous over X-ray diffraction. FTIR is employed to confirm the purity of the samples and presence of metal-oxygen vibrational modes whereas Raman spectroscopy is done to probe local disorder and purity of this synthesized phase. Raman spectroscopy is highly sensitive technique to probe metal-oxygen vibrations and hence a very good probe for studying the local disorder in materials.[27] It has been observed in some cases that Raman spectra provide highly reliable information as far as distinguishing defect fluorite and pyrochlore structures is concerned.[28]

In this study, we wanted to explore the efficiency of $La_2Hf_2O_7$:Pr^{3+} NPs as a potential candidate of lighting and scintillators materials. Therefore, we have synthesized $La_2Hf_2O_7$ NPs with varied Pr^{3+} doping concentrations by a combined co-precipitation and relative low temperature molten salt method. We have taken extensive use of Raman spectroscopy, FTIR, and X-ray photoemission spectroscopy (XPS) for structural, oxidation state and elemental composition studies. In addition, the synthesized NPs were characterized using transmission electron microscope (TEM) and scanning electron microscopy (SEM) to visualize their size and morphology. Moreover, to evaluate their PL and RL properties, optical characterization was carried using steady state luminescence and time resolved PL spectroscopy (TRPLS) exploiting both ultraviolet as well as X-ray radiations. Furthermore, we have performed RL and photon count measurements for X-ray and PL as a function of dopant concentration while optimizing the X-ray excitation power to yield maximum photon count for quantum yield studies. Based on the best of our knowledge, the current study is the most complete report on optical properties of $La_2Hf_2O_7$:x mol%Pr^{3+} NPs under both UV and X-ray excitations.

2. Experimental section

2.1 Synthesis method

All chemicals used in this study are of analytical grade reagents (AR grade) and were used without further purification. The starting materials for the synthesis of the $La_2Hf_2O_7$:Pr^{3+} are as follow: lanthanum nitrate hexahydrate ($La(NO_3)_3$•$6H_2O$, 99.0%), hafnium dichloride oxide hydrate ($HfOCl_2$•$2H_2O$, 99.0%), praseodymium (III) nitrate hexahydrate ($Pr(NO_3)_3$•$6H_2O$,

99.9%), potassium nitrate (KNO_3, 99.9%), sodium nitrate ($NaNO_3$, 98%) and ammonium hydroxide (NH_4OH, 28.0-30.0%). The $La_2Hf_2O_7$:xmol%Pr^{3+} NPs (x = 0.0, 0.1, 0.2, 0.3, 0.5, and 1.0) were prepared by a two-step molten salt process which generates nanoparticles at relatively low temperature as reported by our group and some other groups, such as the synthesis of YAG:Ce and LuAG:Ce, etc.[19,21,29,30,31] First, a single-source precursor was prepared by measuring (5-x) mmol of $La(NO_3)_3$•$6H_2O$ and 5 mmol of $HfOCl_2$•$2H_2O$ and x mmol of $Pr(NO_3)_3$•$6H_2O$ where x is equal to the mol% in respect to the La^{3+} site. The materials were dissolved in 200 ml of 18.2 mΩ Millipore water while simultaneously stirring with a magnetic rod. A titration was set up using 10% diluted ammonium as the titrant and delivered into the metal solution dropwise over a period of 2 hours. The white precipitate formed was vacuum filtrated and washed with DI water until neutral pH. In the next step, the molten salt method was used to ensure size-controlled synthesis of $La_2Hf_2O_7$:xmol%Pr^{3+} NPs via a flux. Specifically, the single-source precursor was mixed with nitrate salts ($NaNO_3$ and KNO_3 in 1:1 molar ratio) and placed in a furnace at 650^{o}C for 6 hours, and followed with washing and purifying with 18.2 mΩ Millipore water and drying. The molten salt method is in particular of interest because it allows for the formation of pure products, even nanoparticles, at relatively low temperatures compare to conventional solid-state method or sol-gel method by forming a flux around the precursor when the salts reach an eutectic point allowing controlled crystal growth and therefore particle size. In addition, the molten salt method ensures no phase transformations due to the low synthesis temperature and allows morphological tunability by controlling the cooling process.[31, 32] In this study, the nanoparticle samples were later annealed for 1 hour at 900 ^{o}C to optimize the optical properties.

2.2 Characterization

Several characterizations were done on the as-synthesized $La_2Hf_2O_7$:xmol%Pr^{3+} NPs. XRD was taken to identify the purity of the as-synthesized NPs by a BRUKER^{TM} D8 Advance X-ray diffractometer with a Cu $K_{\alpha1}$ radiation (λ = 1.5406 Å, 40 kV, 40 mA). The output data were collected from scanning mode in 2θ ranging from 10° to 75° with a scanning step size of 0.04° and a scanning rate of 2.0° min^{-1}. In addition, a Carl Zeiss sigma VP field emission SEM operated at 5 kV was used to record the morphology of the as-synthesized NPs. Furthermore, energy dispersive x-ray (EDX) spectral mapping analysis was performed under 25 kV to record

the composition of the NPs. To further confirm the crystal phase of the as-synthesized NPs, Raman spectra were collected from their power form, using a Bruker Senterra-system with a 785 nm helium-neon laser at a spatial resolution of 2 μm. FTIR spectroscopy was used to identify the metal to oxygen vibrational modes of the NPs by a Thermo Nicolet Nexus^{TM} 470 FT-IR system. XPS was obtained with a 180° double focusing hemispherical analyzer with 128-channel detector using non-monochromatic Al Kα radiation (1486.86 eV) with a power of 240 W (Thermo Scientific™ K-Alpha™ X-ray Photoelectron Spectrometer System). This X-ray source was chosen to minimize the effects of superposition of photoelectron and Auger lines of constituent elements. The diameter of the X-ray beam was ~0.4 mm. The energy resolution of the instrument was chosen to be 0.73 eV, to have sufficiently small broadening of natural core level lines together with a reasonable signal-to-noise ratio. The binding energy scale was calibrated with reference to Cu $3p_{3/2}$ (75.1 eV) and Cu $2p_{3/2}$ (932.7 eV) lines, giving an accuracy of 0.1 eV in any peak energy position determination.

Excitation, emission and lifetime spectra were measured using an Edinburgh Instruments FLS 980 fluorometer system which is equipped with both a steady state source as well as a pulsed source having a frequency range of 1-100 Hz. Lastly, RL was acquired by designing a silver target (λ = 0.52 Å, 60 kV, 200 mA) X-ray tube adaptor to the FLS 980 fluorometer system. Copper metal was used to dissipate heat around the tube by using a half inch-thick sheet. X-ray guider setup was constructed as well to prevent the X-ray beam from scattering and focus to the sample. In addition, protective equipment was constructed to protect the user from radiation by using a 0.75 mm thick lead curtain on a rail to surround the instrument. Additional lead was used in form of sheets to cover the top part of the instrument.

3. Results and discussion

3.1 Phase purity and crystallite size of the $La_2Hf_2O_7$:xmol%Pr^{3+} NPs: X-ray diffraction

Figure 1a shows the XRD patterns of the $La_2Hf_2O_7$:xmol%Pr^{3+} (x = 0.1, 0.2, 0.3, 0.5 and 1.0) NPs. The peaks presented in the XRD data are well define, sharp and intense in nature indicating the high crystalline nature of the as-synthesized NPs. The peak position confirms the fact that the synthesized $La_2Hf_2O_7$:Pr^{3+} NPs were stabilized in cubic fluorite phase with the peaks indexed to (222), (400), (440), and (662) planes. Due to the insensitivity of XRD to the superlattice reflections of pyrochlore phase at (311), (331), (511), and (531) (corresponding to 2θ values of

27°, 36°, 43°, and 50°, respectively), we indexed the XRD peaks to the fluorite phase for the moment while Raman spectra identified their structure differently.[19] In addition, **Figure 1b** shows the variation in XRD peak position corresponding to the most intense (222) peak at 2θ between 28 to 29° as the function of the Pr^{3+} dopant concentration. Furthermore, the lattice parameter *a* was calculated using the Braggs equation with *(hkl)* plane equation to confirm the consistency of the XRD data based on the (222) XRD peak shown in **Figure 1b**. The particle size of the as-synthesized NPs was calculated using Scherer's equation using the full width half max (FWHM) of the (222) plane. The lattice parameter of the $La_2Hf_2O_7$:xmol%Pr^{3+} (x = 0.1, 0.2, 0.3, 0.5 and 1.0) NPs is tabulated in **Table 1**. The crystallite size of the NPs from all doping levels is in nano-size domain. The calculated crystallite sizes are in agreement with both SEM and TEM data presented later in **Figure 3**.

In general, solid solutions follow the Vegards law with the linearity of lattice parameter in accordance with the ionic size of dopant ion and its concentration.[33] From **Table 1**, it can be easily seen that there is not much change in the lattice parameter of the NPs as Pr^{3+} concentration increases from 0.1 to 1.0 mol% because of the similar radii of La^{3+} and Pr^{3+} ions and the low Pr^{3+} doping level.

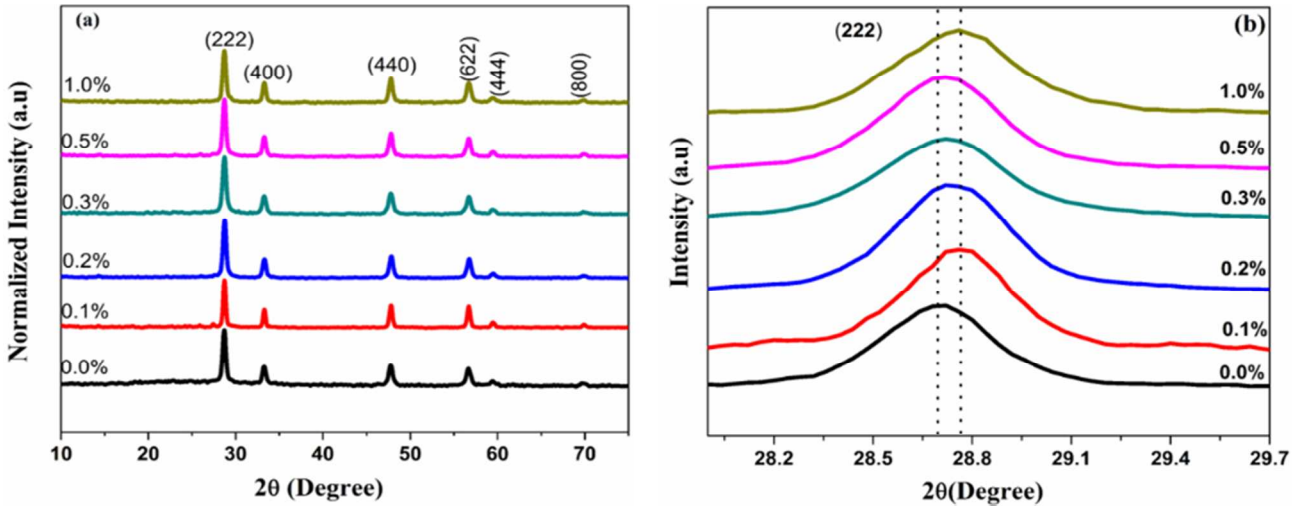

Figure 1. (a) XRD patterns and (b) enlarged view of the XRD peak corresponding to the (222) plane at ~28.72° of the $La_2Hf_2O_7$:xmol%Pr^{3+} NPs (x = 0, 0.1, 0.2, 0.3, 0.5, and 1.0) calcinated at 900 °C.

Table 1. Lattice parameter of the $La_2Hf_2O_7$:xmol%Pr^{3+} NPs as a function of dopant concentration (x = 0, 0.1, 0.2, 0.3, 0.5, and 1.0)

Pr^{3+} doping concentration (%)	2θ (°)	FWHM (β)	Lattice parameters (Å)
0.00	28.69	0.24	10.77
0.10	28.72	0.11	10.76
0.20	28.73	0.20	10.75
0.30	28.71	0.26	10.76
0.50	28.70	0.21	10.76
1.00	28.71	0.22	10.76

3.2 Raman analysis

In literature, it is well known that the cubic pyrochlore structure processes total of six Raman active modes which according to group theory are $\Gamma = A_{1g} + E_g + 4F_{2g}$,[34, 35] while the defect fluorite structure has only one active mode F_{2g}. The Raman spectrum of fluorites phase mainly display single broad peak because seven O^{2-} ions are randomly distributed over the 8 anionic sites in this structure giving rise to significant disordering. In **Figure 2,** for pure $La_2Hf_2O_7$ we could clearly identify five Raman active modes pertaining to the vibrations of Ln-O and Hf-O bonds at around 304, 321, 402, 499 and 522 cm^{-1} which are assigned to F_{2g}, E_g, F_{2g}, F_{2g}, and A_{1g}, respectively.[36] The sixth Raman mode at 600 cm^{-1} (F_{2g} band) is not found from our samples, as it is often reported that this particular band is absent in many pyrochlores .[37] The vibrational modes at lower frequencies region (300-400 cm^{-1}), i.e. the F_{2g}, E_g, and F_{2g} modes, arise from vibrations of the La–O and Hf–O bonds. On the other hand, the higher frequency band (522 cm^{-1}) of A_{1g} arise due to the stretching of the Hf–O bonds while the small kink around 710 cm^{-1} is ascribed to the distortion of HfO_6 octahedral .[36] The acquired Raman spectra suggest that the crystal phase of the synthesized $La_2Hf_2O_7$:xmol%Pr^{3+} NPs is indeed in the pyrochlore phase and not in the defect fluorite structure as suggested by the XRD data. The pyrochlore structure of $A_2M_2O_6O'$ composition is composed of two varieties of chemical bonds, where the M-O bonds are relatively covalent and A-O bonds are much weaker. The strongest band is located at 304 cm^{-1} that can be attributed to the F_{2g} internal La-O stretching mode. The presence of Raman band at ~260 cm^{-1} can be ascribed to two reasons: (i) doping induced peak splitting of the F_{2g} band at 304 cm^{-1} and

(ii) A_g translatory mode of Pr-O bond. According to Hooke's law, vibrational frequency is inversely proportional to effective mass. Since Pr is heavier than La, vibration of Pr-O bond is at lower wavenumber compare to that of La-O bond. The bond length of Pr-O is actually longer than that of La-O, which causes the distance of oscillation to increase, therefore the energy and wavenumber to decrease. The peak at 402 cm^{-1} is red shifted to 374 may also be attributed to doping effect wherein vibration of Pr-O interferes with La-O bond vibration and cause splitting and shifting of Raman band. The blue shift is the result of higher effective mass of Pr-O than La-O.[38] Overall, the use of Raman spectroscopy confirmed that the as-synthesized $La_2Hf_2O_7$:xmol%Pr^{3+} NPs possess the pyrochlore structure, a phase essential to the explored applications.

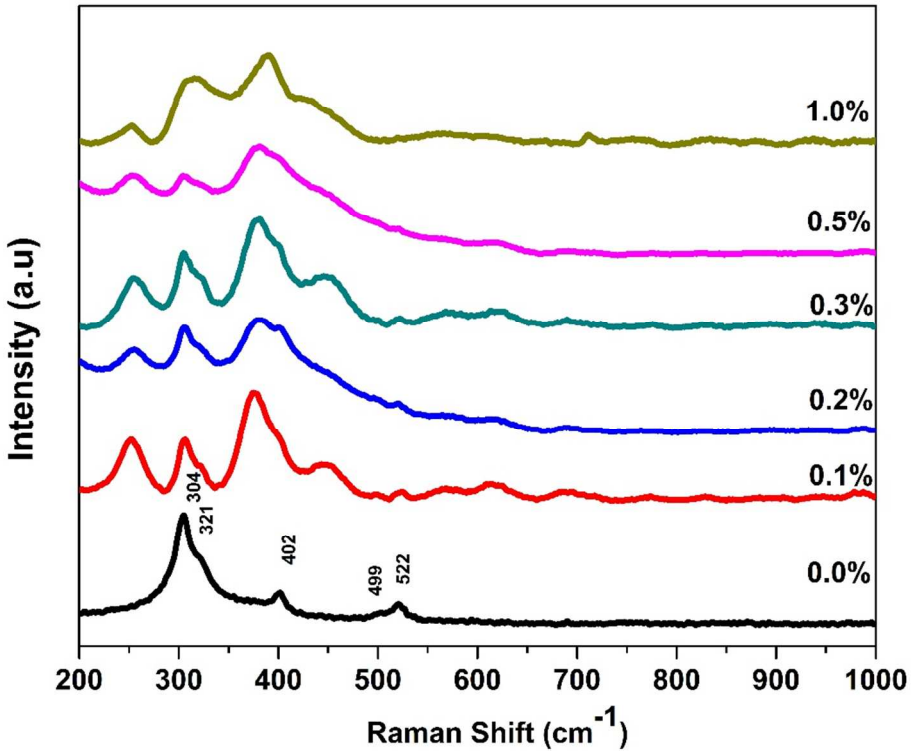

Figure 2. Raman spectra of the $La_2Hf_2O_7$:xmol%Pr^{3+} (x = 0, 0.1, 0.2, 0.3, 0.5, and 1.0) NPs after calcinated at 900 ^oC.

3.3 Infrared Spectroscopy

FTIR spectroscopy was used to confirmed the composition of the $La_2Hf_2O_7$:xmol%Pr^{3+} NPs in which the ratio of the pellet made for analysis was 1:10 in weight of the $La_2Hf_2O_7$:xmol%Pr^{3+} sample to KBr (**Figure S1)**. Pyrochlore oxides ($A_2B_2O_7$) are known to possess seven IR active modes in the range of 750–50 cm^{-1} originating from vibration and bending of A-O and B-O

bonds .[39] The IR band (v_1) at around 623 cm^{-1} is attributed to Hf^{IV}-O stretching mode in the HfO_6 octahedron and the second band (v_2) around 519 cm^{-1} is attributed to La^{III}-O stretching mode. In addition, the inset of **Figure S1** shows the full range in which the data was collected, proving the absence of peaks corresponding to hydroxyl, nitrogen, or inorganic salts used during the molten salt synthesis showing the purity of the $La_2Hf_2O_7$:xmol%Pr^{3+} NPs after calcination. On doping Pr^{3+} ion in $La_2Hf_2O_7$ NPs we could not find much difference in the FTIR spectral pattern, suggesting the all samples had similar composition.

3.4 XPS analysis

XPS can be used to determine the chemical state/oxidation state of the elements and the surface composition of the annealed samples. **Figure S2** depicts the XPS spectra of La 3d, Hf 4f, O 1s and Pr 3d of the $La_2Hf_2O_7$:xmol%Pr^{3+} NPs. La 3d XPS spectra of the NPs and the binding energies (BE) of La $3d_{5/2}$ and La $3d_{3/2}$ at 837 and 854 eV in addition to 841 and 858 eV La 3d satellite peaks are presented in **Figure S2a**. La 3d X-ray photoelectron peak not only splits into $3d_{5/2}$ and $3d_{3/2}$ due to a spin–orbit coupling but additionally, each of these lines splits further due to a transfer of an electrons from oxygen ligands to the La 4f orbital.[40] The difference in energy between the $3d_{3/2}$ and $3d_{5/2}$ states is approximately 17 eV. The value of BE and the XPS peak splitting agree well with reported values for the La^{3+} compounds which confirms the +3 oxidation state of lanthanum ions in our NPs.[41, 42] On doping Pr^{3+} ion, it can be seen that both peaks shifted to higher BE values which can be attributed to different chemical surrounding around La^{3+} ions. On the other hand, most reports [43-45] depict clear splitting in Hf 4f peak to $4f_{7/2}$ and $4f_{5/2}$ similar to our observation. Fitting the curves of Hf 4f core levels (**Figure S2b**) show two typical peaks in pure $La_2Hf_2O_7$ at BE = 17.18 eV and BE = 19.07 eV, corresponding to $4f_{5/2}$ and $^4f_{7/2}$ with 4f spin-orbit splitting energy calculated to be ~1.89 eV. Hf $4f_{7/2}$ peak at BE = 19.07 eV indicates the formation of Hf–O bonding and Hf^{4+} oxidation number. As a function of dopant ion concentration, this doublet of Hf-4f peaks shifts towards higher BE and the shift increases with increasing Pr^{3+} concentration. Compare to La 3d, the increase in shift is more obvious because the bond length of La-O is greater than that of Hf-O in $La_2Hf_2O_7$.

Furthermore, the standard BE from the photoelectrons of Pr $3d_{5/2}$ in elementary substance is 931.9 eV (±0.1 eV) and in Pr_2O_3 is 933.2 eV (±0.1 eV),[46] which is very different from the experimental data of observed BE at 938 eV in this study (**Figure S2c**). The large shift in BE

values indicates the formation of Pr-O-La/Hf clusters in the $La_2Hf_2O_7$:xmol%Pr^{3+} NPs. Due to lower electronegativity of Pr compared to that of La, the electron cloud around Pr is much closer to oxygen in Pr-O-La bond than the electron cloud from La, which results in a higher binding energy component of Pr in our samples compared to that of Pr in Pr_2O_3 at 933.4 eV.

In addition, it is well known that oxygen ions and oxygen vacancies are distributed across all anion sub-lattice sites in $Ln_2M_2O_7$ compounds. With the addition of Pr^{3+} to the host it can be observed, both the oxygen ions and vacancies being rearranged or destroyed through the lattice. It can be observed from **Figure S2d** that the undoped $La_2Hf_2O_7$ has binding energies of ~530.0 and 531.85 eV and a shift towards higher BE from the $La_2Hf_2O_7$:xmol%Pr^{3+} NPs as the doping percentage of Pr^{3+} increases. In general, the O 1s profile is more complex due to the overlapping contribution of oxygen from La and Hf. Six out of every seven oxygen ions occupy the 48f sites and each is coordinated by two lanthanum and two hafnium ions, and the seventh oxygen ion occupies the 8b site and is surrounded by four hafnium ions. This means that the electron density on oxygen for the La-O bond is higher than that of Hf-O bond, which could be the most possible reason for having two binding energy peaks for O 1s in the $La_2Hf_2O_7$:0.1%Pr^{3+} crystal structure.[47] The O1s spectra is clean indicating that nitrogen is not present after the molten salt synthesis. In fact, if nitrogen were present oxygen peaks from N-O bond would be present. Overall, the broadness of the peaks indicate that oxygen is distributed uniformly throughout the lattice structure.

3.5. Morphological study: scanning and transmission electron microscopies

SEM images of the undoped and Pr^{3+} doped $La_2Hf_2O_7$ NPs annealed at 900 ^{O}C are shown in **Figure 3a-f**. The undoped as well as Pr^{3+}-doped $La_2Hf_2O_7$ NPs are spherical in shape and monodisperse at low doping level. The morphology of the NPs does not seem to vary too much as a function of dopant ion concentration. At highest doping concentration grain, distribution reveals slight agglomeration, which still needs to be, confirmed (**Figure 3f**). The average size of the particles is 25-50 nm for most of the samples. TEM study was carried on the $La_2Hf_2O_7$:1.0%Pr^{3+} NPs with maximum Pr^{3+} doping concentration to see whether indeed any agglomeration exist in the sample (**Figure 3g**). The observed monodisperse NPs confirmed the advantage of our combined co-precipitation and molten salt synthesis procedure. Lastly, TEM

also depicted that particles are more or less spherical in nature and the particle size is around 35 nm which is in close agreement with the calculated size from the XRD data (**Figure 1**).

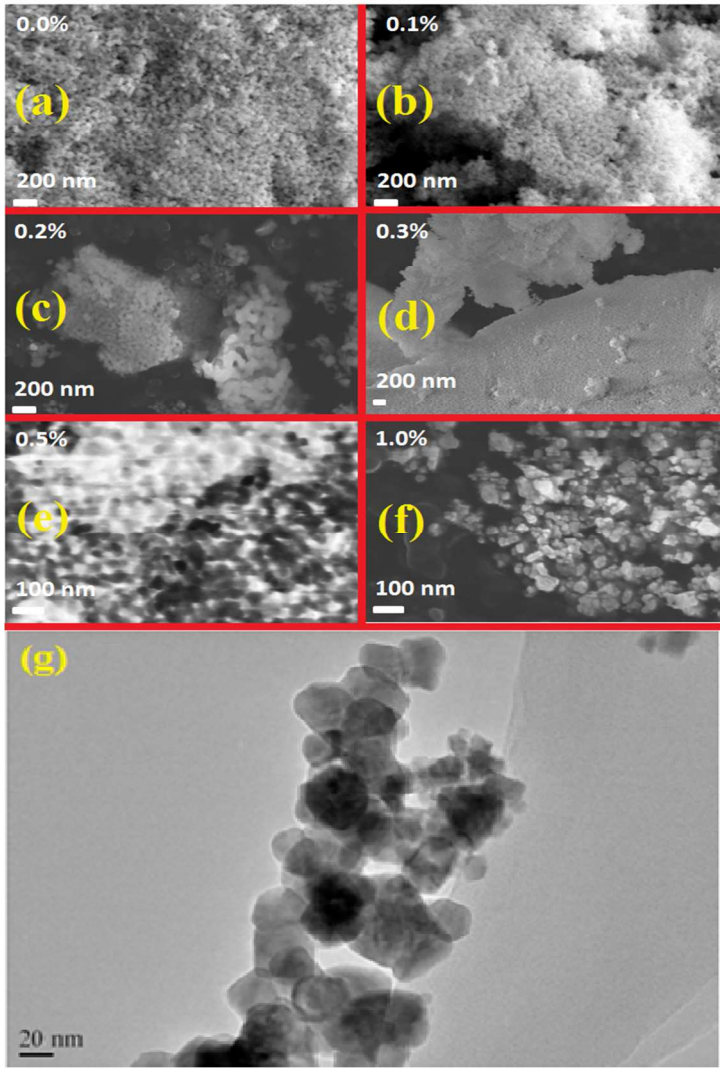

Figure 3. (a-f) SEM micrographs of the $La_2Hf_2O_7$:xmol%Pr^{3+} (x = 0, 0.1, 0.2, 0.3, 0.5, and 1.0) NPs. (g) TEM micrographs of the $La_2Hf_2O_7$:1.0%Pr^{3+} NPs.

3.5 Photoluminescence: Optical properties under UV excitation

PL characterizations were done to understand the excitation, emission and lifetime decay of the $La_2Hf_2O_7$:Pr^{3+} NPs. **Figure 4a** shows the excitation spectra of the $La_2Hf_2O_7$:Pr^{3+} NPs displaying features, which are characteristics of 4f-5d and 4f-4f transition of trivalent praseodymium ion. The broad band in the range 225-275 nm is attributed to inter-configurational transition 4f-5d transition. The peaks at 443, 459 and 488 nm (displayed in the inset of Figure 5a) are ascribed to

$^3H_4 \rightarrow {}^3P_2$, $^3H_4 \rightarrow {}^3P_1$ and $^3H_4 \rightarrow {}^3P_0$ f→f transitions of Pr^{3+}ions, respectively. Not much change in spectra could be seen as a function of dopant concentration.

Pr^{3+} ions have two possible transitions, i.e. La-Porte forbidden intra-configurational 4f-4f and allowed 4f-5d inter-configurational transitions. [48]The emission spectra of the $La_2Hf_2O_7$:x%Pr^{3+} NPs under 255 nm excitation is shown in **Figure 4b**. The emission spectra at various Pr^{3+} concentrations displayed the same spectral features. The peaks at 490, 534, 632, 662 and 727 nm correspond to the $^3P_0$-$^3H_4$, $^3P_0$-$^3H_5$, $^3H_5$, $^3P_0$-$^3F_2$ and $^3P_0$-$^3F_3$ transitions of Pr^{3+}, respectively. The emission peak around 603 nm is attributed to $^1D_2$-$^3H_4$ transition. Normally visible light emission from 4f→4f transition of Pr^{3+} doped inorganic hosts is mostly seen from $^3P_0$ and $^1D_2$ states. Based on the strength of the crystal field a host lattice offers, there may be variation in relative intensity of emission from these two states since the crystal field of the matrix materials determines where the bottom of the $4f^5d$ level of Pr^{3+} going to lies with respect to $^3P_0$ and $^1D_2$ states.[49] Whether emission comes from $^3P_0$ state or $^1D_2$ state or from both of them completely depends on the kind of hosts. Our literature survey shows that only green emission from $^3P_0$ could be seen in $CaZrO_3$ perovskite [50] whereas Pr^{3+} doping displayed only red emission from $^1D_2$ states in RE_2O_3 (RE = Sc, Y, Gd) and Lu_2O_3 [51, 52].

The relative intensities of emission from $^3P_0$ and $^1D_2$ states depends on various photophysical phenomena, such as multiphonon relaxation, cross-relaxation, intersystem crossing (ISC) through low-lying $4f^15d^1$ levels, and charge transfer (CT) mechanism, etc.[53] Nature of the host plays a role as well in deciding the intensity ratio of blue/green and red emissions from $^3P_0$ and $^1D_2$ states, respectively, as the position of charge transfer state (CTS) is dependent on the same. For the oxide-based host, it is normally localized around excited states of lanthanide ion.[54] Emission quenching from $^3P_0$ state of Pr^{3+} ions depends on the spectral position of the CTS with respect to $^3P_0$ and $^1D_2$ states.[54] It is reported that blue/green emission was more intense than red emission in CaTiO3 whereas red emission is more intense than green emission in cases of $Na_5La(WO_4)_4$, $Na_5Y(WO_4)_4$, $CaTa_2O_6$, and $La_2Ti_2O_7$ and $Gd_2Ti_2O_7$ type pyrochlore structure.[52, 54,55] Our $La_2Hf_2O_7$:Pr^{3+} NPs could emit both intense greenish-blue ($^3P_0 \rightarrow {}^3H_4$) and red ($^1D_2 \rightarrow {}^3H_4$) emissions, which are important for inorganic phosphors. It seems replacing Ti^{4+} by Hf^{4+} in pyrochlore structure changes the green to red ratio due to the difference in the crystal field induced by HfO_6 octahedra compared to TiO_6 one. $La_2Hf_2O_6$ pyrochlore has two cationic sites 8-coordinated La^{3+} (scalenohedra) and 6-coordinated Hf^{4+} sites (octahedra). In our

$La_2Hf_2O_7$:Pr^{3+} NPs the origin of emission from both $^3P_0$ and $^1D_2$ states is attributed to stabilization of Pr at both lanthanum site as well as Hf^{4+} site. For divalent and trivalent lanthanide ions, the difference in energy between the 4f5d and 4f states is inversely proportional to crystal field strength of the host matrix, which in turn increases as the distance between the lanthanide ion and the ligands decreases.[49] Since La-O bond (0.264 nm) is longer than Hf-O bond (0.208 nm) the effect of ligand on Pr^{3+} at lanthanum site will be less compared to that at Hf site. Therefore, the emission from $^3P_0$ level arises because of fraction of Pr^{3+} localized at Hf^{4+} whereas the one from $^1D_2$ arises due to the rest of Pr^{3+} being stabilized at La^{3+} site, however stabilization of Pr^{3+} at Hf^{4+} may leads to generation of large concentration of oxygen vacancies.[21]

Quantum yield was acquired by using an integrating sphere in our FLS 980 system and the results was shown in **Figure 4c**. The $La_2Hf_2O_7$:0.1%Pr^{3+} NPs were found to possess the strongest emission intensity with a quantum yield (QY) of 20.54 ± 0.1%. Beyond 0.1% Pr^{3+} doping level, the emission intensity and QY was found to decrease which is attributed to concentration quenching. The problem of concentration induced fluorescence quenching even at low Pr^{3+} concentrations is a well-known issue even though efficient luminescence in phosphors doped with high concentration of Pr^{3+} is reported quite often.[56] The concentration quenching is attributed to non–radiative energy transfers (ET) between two Pr^{3+} ions at high concentrations when they are at closed distance known as critical distance. Non-radiation transition arises mainly because cross-relaxation ET from one Pr^{3+} to the closed by another one. Based on Pr^{3+} energy level diagram, the difference in energy between the $^3P_0$ and $^3H_6$ states is approximately around 16,000 cm^{-1}, and the one between the $^3H_4$ and $^1D_2$ level is close to16,700 cm^{-1}.[48, 57] Concentration quenching in this case is mainly induced mainly by cross-relaxation process between neighboring Pr^{3+} ions.[58] Based on critical distance one can predict the mechanism of concentration quenching.

Colorimetric performance of the $La_2Hf_2O_7$:0.1mol%Pr^{3+} NPs, i.e. those with maximum emission output and QY, was established using the color coordinates calculated using the intensity-corrected emission spectra excited by 255 nm with respect to monochromator, source and detector. The calculated CIE color coordinates for the $La_2Hf_2O_7$:0.1%Pr^{3+} NPs are found to be 0.433 and 0.370, which are located in the color coordinated CIE diagram and confirm the reddish yellow emission from the Pr^{3+} doped lanthanum hafnate NPs (on the boundary line of CIE white domain), as shown in **Figure 4d.** In respect to the previous emission profile (Figure 5b) and

proceeding radioluminescence data (Figures 7 and 8), both optical test agrees with the quantum yield results proving the 0.1% Pr^{3+} doped $La_2Hf_2O_7$ sample was the most efficient one among all our samples.

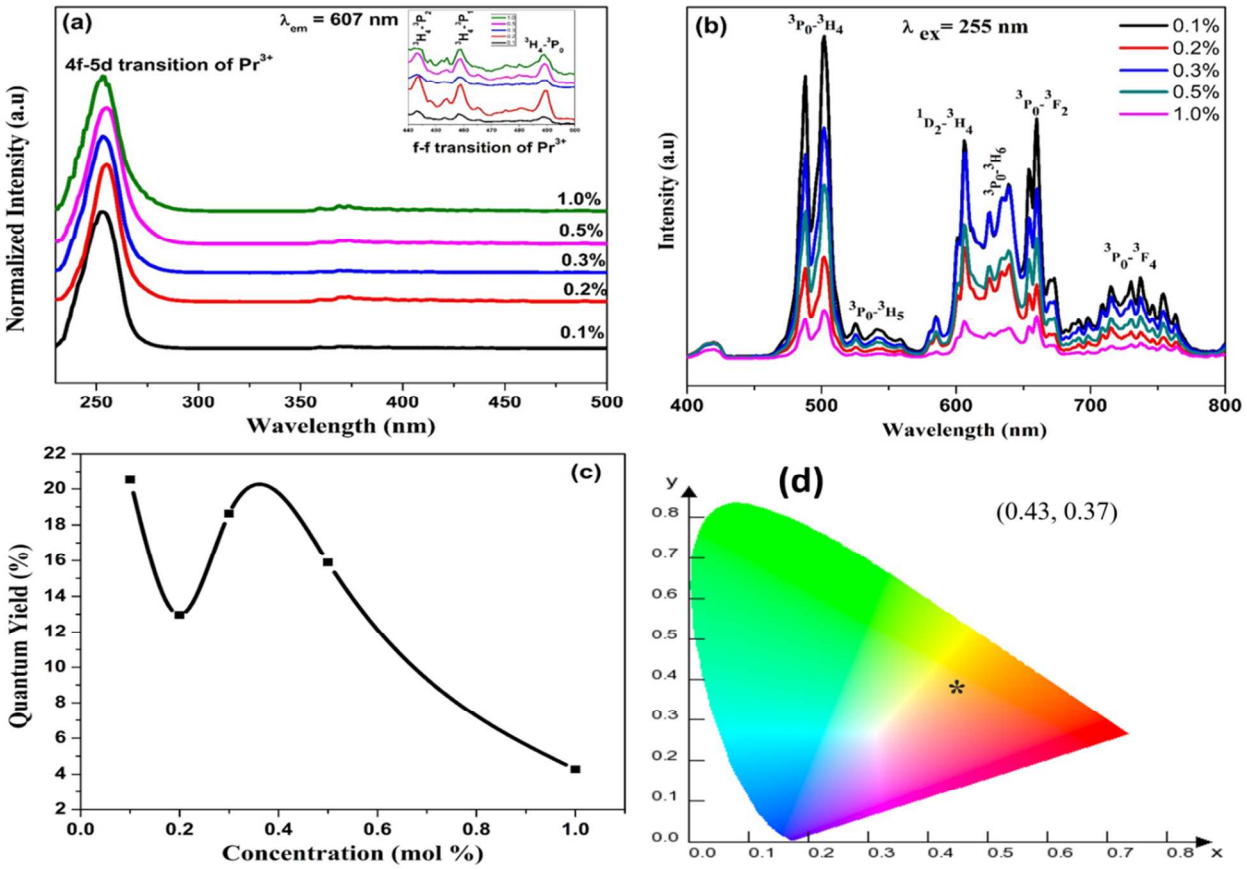

Figure 4. (a) Excitation and (b) emission spectra, and (c) quantum yield as a function of the Pr^{3+} doping concentration of the $La_2Hf_2O_7$:x%Pr^{3+} (x = 0.1, 0.2, 0.3, 0.5, and 1.0) NPs. (d) CIE color coordinate diagram of the $La_2Hf_2O_7$:0.1%Pr^{3+} NPs.

The lifetime studies of the $^1D_2 \rightarrow {}^3H_4$ transition (607 nm) of Pr^{3+} ions in the $La_2Hf_2O_7$:x%Pr^{3+} NPs were performed using pulsed Xenon lamp at 255 nm excitation shown in **Figure 5a**. Decay profiles displayed non-exponential behavior, however the $^1D_2$ level decays by three different processes: radiative decay ($^1D_2 \rightarrow {}^3H_4$), multiphoton relaxation ($^1D_2 \rightarrow {}^1G_2$), and cross-relaxation induced energy transfer ($^1D_2 \rightarrow {}^3H_4/{}^3H_4 \rightarrow {}^3F_{3,4}$).[54] This non-exponential behavior is mainly due to cross-relaxation and luminescence quenching. Cross-relaxation is a photophysical phenomenon wherein excitation energy from an ion decaying from a highly excited state promotes a nearby

ion from the ground state to the metastable level. In this case, the non-exponential decay profiles were fitted by bi-exponential equation:

$$I(t) = A_0 + A_1 \exp\left(\frac{-t}{\tau_1}\right) + A_2 \exp\left(\frac{-t}{\tau_2}\right)$$

Where I(t) is PL intensity, τ_1 and τ_2 are emission decay times, and A_1 and A_2 are their relative weightages. As can be seen from **Table 2**, two life time values were observed for Pr^{3+} in the order of 170-310 μs (T_S, short lifetime) and the other one in the range 570-960 μs (T_L, longer lifetime). As a function of dopant concentration the lifetime values (both) initially increase with increasing Pr^{3+} ion concentration till 0.2mol%, but beyond that dopant level, the lifetime values start falling (**Figure 5b**). In most of the literature reported on Pr^{3+} doped phosphor materials, lifetime's values are in the range of nanoseconds to 50 μs. In our case, the lifetime values are exceedingly high. The average value is 814 μs for the $La_2Hf_2O_7$:0.2mol%Pr^{3+} NPs.[59] This suggests that Pr^{3+} ion is not homogenously distributed in the $La_2Hf_2O_7$ host. When the activator ions have different local sites, they are likely to relax at different transition rates. If the rates of relaxations are very distinct, then different decays coexist for these activator ions. Assuming a given phonon energy here because Pr^{3+} ions are localized in the same $La_2Hf_2O_7$ host, the relatively longer lived Pr^{3+} ions (570-960 μs) are ascribed to a relatively symmetric site/environment as 4f-4f transition are optically forbidden in site with inversion symmetry, whereas the short lived Pr^{3+} ions (170-310 μs) are more likely to arise from those occupying an asymmetric site, wherein the selection rules get relaxed. In $La_2Hf_2O_7$ pyrochlore, Pr^{3+} ions are more likely to be stabilized at two sites: symmetric La^{3+} site (S1) with regular LaO_8 polyhedral and relatively asymmetric Hf^{4+} site (S2) with HfO_6 distorted octahedral. Fast decaying species (170-310 μs) T_S arises because of Pr^{3+} ions occupying the Hf^{4+} (S2) site without inversion symmetry, whereas slow decaying species T_L can be attributed to Pr^{3+} ions occupying the La^{3+} (S1) site with inversion symmetry. Such site selective luminescence spectroscopy for rare earth ion (Eu, Sm, Dy, and Tb) has been reported in many hosts.[59-64] However, we cannot rule out the contribution of cross-relaxation and fluorescence quenching on this phosphor for the non-exponential decay.

Table 2. Luminescence lifetime data of the $La_2Hf_2O_7$:xmol%Pr^{3+} NPs (λ_{ex} = 255 nm and λ_{em} = 607 nm) at various dopant ion concentrations (x = 0.1, 0.2, 0.3, 0.5, and 1.0)

Pr^{3+} doping concentration (%)	τ_1 (µs)	τ_2 (µs)
0.10	277.2	781.3
0.20	308.3	959.1
0.30	299.1	877.6
0.50	277.5	856.7
1.00	170.0	572.8

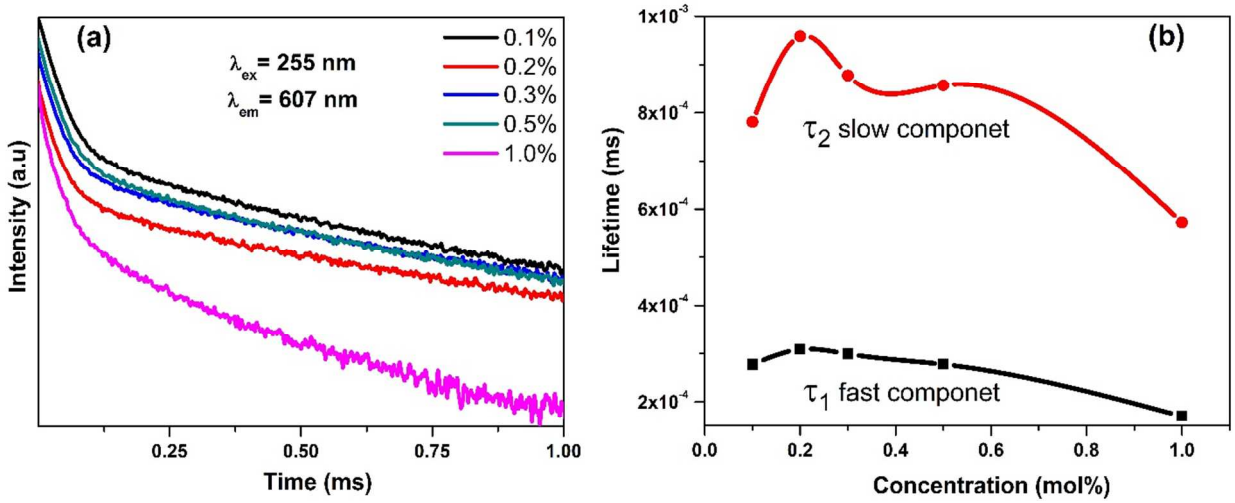

Figure 5. (a) Luminescence decay profiles and (b) variations of luminescence lifetimes of the $La_2Hf_2O_7$:xmol%Pr^{3+} (x = 0.1, 0.2, 0.3, 0.5, and 1.0) NPs at λ_{ex} = 255 nm and λ_{em} = 607 nm.

3.6 Radioluminescence: Optical properties under X-ray excitation

The $La_2Hf_2O_7$:x%Pr^{3+} NPs have an interesting lattice for scintillators. Considering the high density (7.8 gm/cm^3) and the potential of lanthanum hafnate materials as a scintillator,[21] X-ray exited luminescence (XEL) spectra were taken on these NPs. As shown in **Figure 6a**, the XEL spectra look very similar to photon VUV and UV excited luminescence. In addition, there was not much change as a function of dopant concentration too. Marginal variation could be ascribed to sensitivity of the used PMT. The RL emission spectra (**Figure 6a**) display typical characteristics of Pr^{3+} ion with peaks position similar to one seen under photoluminescence (**Figure 4b**). As such, X-ray excitation is different from UV excitation since under X-ray excitation e^--h^+ pairs are generated and Pr^{3+} 4f-5d/4f-4f bands and hosts were excited together. In this situation, e^- is migrating to Pr^{3+} centers whereas under UV, only Pr^{3+} (4f-5d/4f-4f) bands were excited but not the host. As discussed, Pr^{3+} ions are distributed at both La^{3+} and Hf^{4+} sites in lanthanum hafnate. For $La_2Hf_2O_7$, the valence bands (VB) is composed of O 2p orbitals

hybridized with Hf 5d orbitals along with a minor contribution from La 4f states. On the other hand, conduction band (CB) is mainly composed of La 4d states (in majority spin component), 4f states (in minority spin component) and Hf 5d states. Hf 5d states contribute solely in the lower part of the conduction band.[65] The Pr^{3+} ion occupying tetravalent hafnium sites may leads to negative antisite defect (Pr'_{Hf}) as well as a positive defect ($V_{\ddot{O}}$) as indicated below.

$Pr^{3+} + Hf^{4+} \rightarrow Pr'_{Hf} + V_{\ddot{O}}$

Moreover, this Pr'_{Hf} defect is XEL active and amenable to emission under X-ray excitation. This is similar to what Dobrowolska *et al* have observed in barium hafnate doped with europium io.[66] Excitation with 12W energetic X-ray beam leads to formation of an exciton (bound electron-hole pair) between an electron in the lower part of the CB comprising of Hf 5d states ($5d^1$ Hf^{3+}) and a hole in the VB if they possess similar momentum. The next step is transfer of excitons energy to Pr'_{Hf} luminescent center followed by emission of the luminescent ions that radiatively return from an excited state to the ground state. The XEL arises from both $^3P_0$ and $^1D_2$ states around 472-512 nm ($^3P_0 \rightarrow {}^3H_4$) and 595-635 nm ($^1D_2 \rightarrow {}^3H_4$), respectively. The dependence of XEL intensity on dopant concentration follows a similar trend as PL and the highest intensity was found to be at 0.1% doping level (**Figure 6b**). The PL and XEL emission profile looks quite similar, which indicates the same radiative levels, are involved in emission in visible region in both cases.

Looking out for Pr^{3+}-activated oxide based phosphor materials and their application as scintillators for X-ray computed tomography requires chemical modifications which requires the fast decaying $^3P_0 \rightarrow {}^3H_4$ transition (in μs range) to be more intense than the slow decaying $^1D_2 \rightarrow {}^3H_4$ transition (in ms range). On the other side, solid-state lighting applications require the dominance of the $^1D_2 \rightarrow {}^3H_4$ emission over that of the $^3P_0 \rightarrow {}^3H_4$ transition. Here we could get emission from both states though red emission from $^1D_2$ states is more dominant than $^3P_0$ state from our samples. The more fraction of the $^1D_2$ in our XEL spectrum is not very advantageous as this has much longer decay time. From the XEL spectrum we can decipher that lanthanum hafnate activated with Pr^{3+} ions can convert the incoming high energy X-ray photon into low energy visible light. The mechanism of XEL is depicted in **Figure 6c**. In the present case though XEL efficiency is rather low, our results are still encouraging enough to give a direction wherein we could modify the pyrochlore lattice to enhance the emission from $^3P_0$ states. It is connected

with the nature of Wannier-Mott type excitons in $La_2Hf_2O_7$ which exist for oxide with high dielectric constant.[67, 68] They are weakly bonded and have large radii and are known as large exciton and as a result, on collisions with phonons they easily get destructed.[66] Because of this, the number of excitons formed during X-ray excitation in case of $La_2Hf_2O_7:Pr^{3+}$ is relatively lower in magnitude than in materials where Frenkel type excitons are formed. The exciton-exciton interactions are less probable due to their lower mobility that results in lower probability of energy transfer and less luminescence intensity.

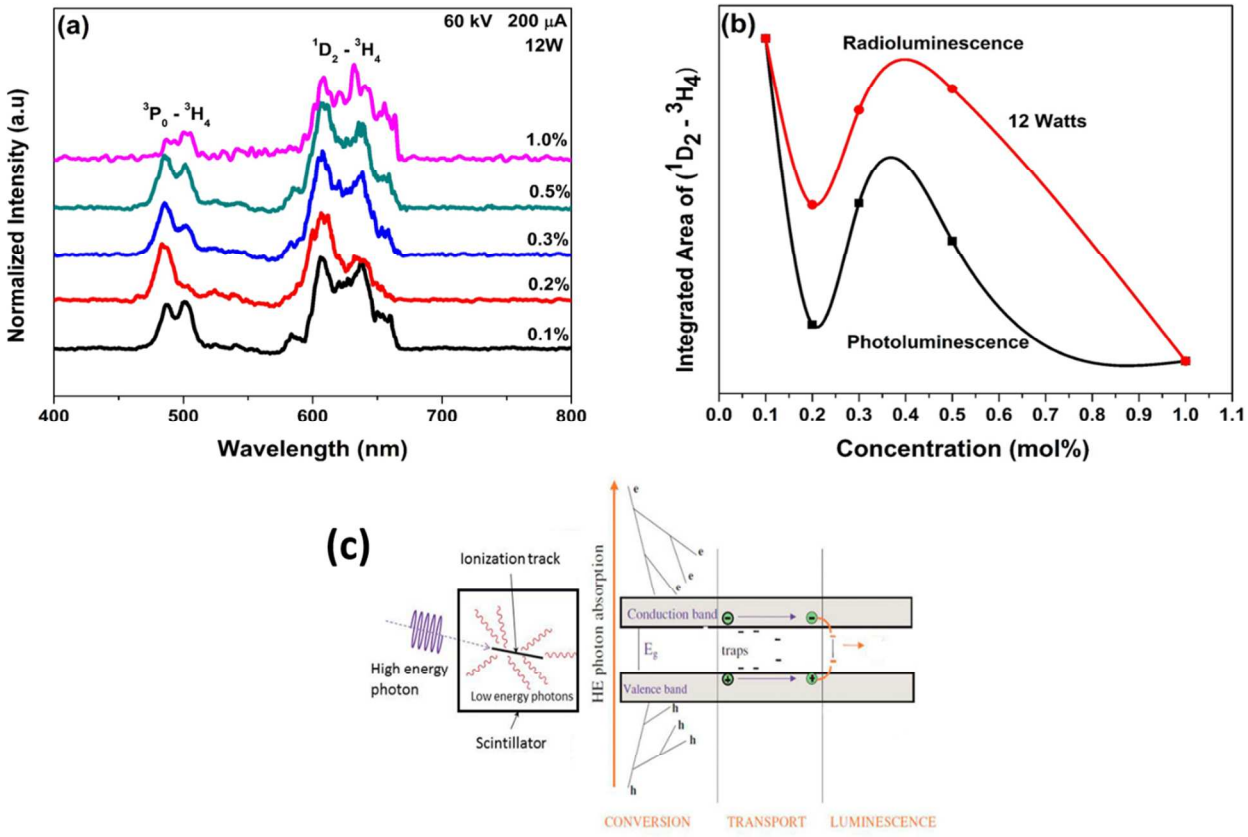

Figure 6. (a) XEL spectra and (b) comparison of concentration dependence of XEL and PL intensities as a function of dopant concentration of the $La_2Hf_2O_7:x\%Pr^{3+}$ NPs. (c) Scintillation mechanism of doped materials.

Lastly, X-ray dosage dependence study was conducted to determine the best emission output with respect to the power (**Figure 7a**). The $La_2Hf_2O_7:0.1\%Pr^{3+}$ NPs were used in this study due to its outstanding emission performance over other samples. This is important to understand because it allows to differentiate the durability and performance when exposed at different

powers of radiation. It was found that the maximum emission output was acquired at 12 watts (**Figure 7b**).

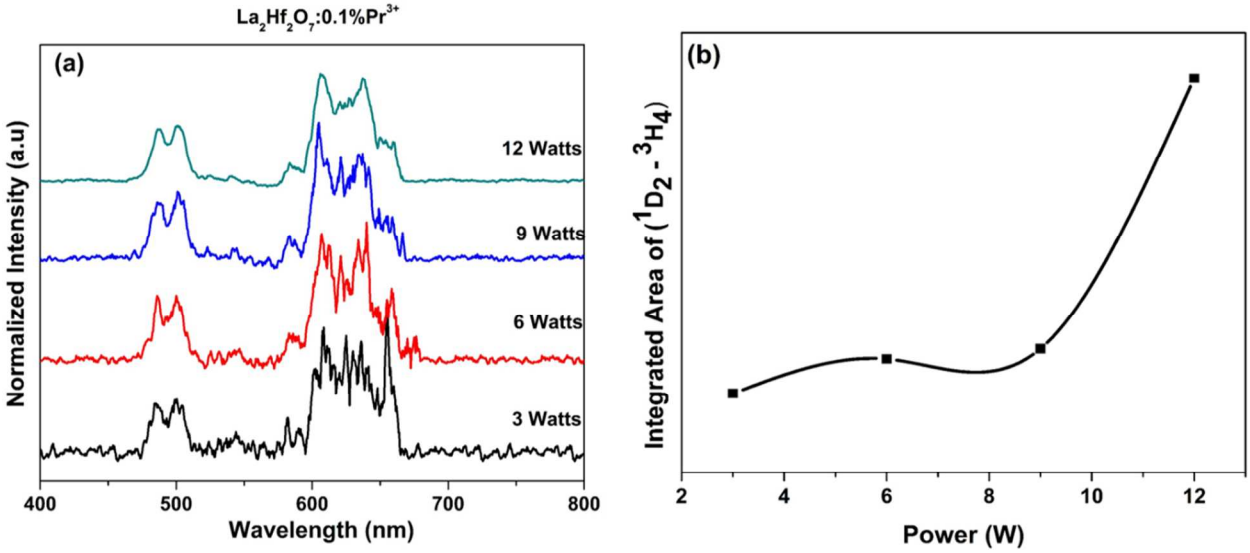

Figure 7. (a) XEL spectra and (b) variation of emission output from the $^3P_0 \rightarrow {}^3H_4$ transition of Pr^{3+} ion of the $La_2Hf_2O_7$:0.1%Pr^{3+} NPs at various X-ray powers.

Furthermore, $La_2Hf_2O_7$ is a material with high dielectric constant and excitons formed in these cases on exposure to ionizing radiation such as X-ray are weakly bonded known as Wannier-Mott type excitons (WMEs). They break easily on collision with phonons. The number of excitons thus available for energy transfer to Pr^{3+} ion will be less and hence low RL output as shown in Figures 6a and 7a. On the other hand, under UV excitation with 255 nm, the $La_2Hf_2O_7$ host absorbs the energy and transfer to radiative Pr^{3+} centers directly. This is known as host sensitized energy transfer. That is why the emitted photon counts corresponding to green and red emission under the UV excitation (Figure 4b) are larger than the ones excited by X-ray.

4. Conclusion

In this study, $La_2Hf_2O_7$:x mol%Pr^{3+} NPs (x = 0, 0.1, 0.2, 0.3, 0.5, and 1.0) were synthesized using a molten salt synthesis and systematically characterized using XRD, Raman, FTIR, XPS, SEM, TEM and UV/ X-ray excited optical luminescence. Raman spectroscopy confirmed the presences of six metal-oxygen vibrational modes typical of ordered pyrochlores phase while XPS reflected

the formation of oxygen vacancies due to stabilization of a fraction of Pr^{3+} ions at Hf^{4+} sites. The presence of La-O and Hf-O vibration bonds was confirmed through FTIR spectroscopy. The spherical shape of these NPs was confirmed from SEM and TEM, which also confirmed the formation of $La_2Hf_2O_7:Pr^{3+}$ nanodomains. Photoluminescence data revealed the presence of green and red emissions due to the $^3P_0 \rightarrow {}^3H_4$ and $^1D_2 \rightarrow {}^3H_4$ transitions. However, the emission from $^1D_2$ states was found to be more intense than that from $^3P_0$ states. This phenomenon has a huge implication in the design of novel phosphor for possible applications in solid-state lighting. Colorimetric performance of the $La_2Hf_2O_7$:0.1mol%Pr^{3+} NPs confirmed the reddish yellow emission from $^3P_0$ level due to f Pr^{3+} ions localizing at Hf^{4+} sites. On the other hand, emission from $^1D_2$ states arises from the Pr^{3+} localized at La^{3+} site. In addition, the $La_2Hf_2O_7$:0.1mol%Pr^{3+} NPs were found to possess the strongest emission intensity with a quantum yield of 20.54 ± 0.1%. However, beyond 0.1% Pr^{3+} doping level, the emission intensity and QY of the $La_2Hf_2O_7$:x%Pr^{3+} NPs were found to decrease which is attributed to concentration quenching. Lifetime spectroscopy pin-pointed that the fast decay in the range of 170-310 μs arises because some Pr^{3+} ions occupy Hf^{4+} sites whereas the slow decay in the range of 570-960 μs can be attributed to Pr^{3+} ions occupying La^{3+} sites. X-ray induced optical luminescence depicted intense green and red emissions arising from $^3P_0$ and $^1D_2$ states of Pr^{3+} ion. The effect of changing X-ray power on radioluminescence was also explored and we could see monotonically increased intensity as a function of X-ray power. All together, we developed and investigated a series of $La_2Hf_2O_7$:xmol%Pr^{3+} NPs in this work with exciting results not only for luminescence applications but also opening a new gateway for doped pyrochlores NPs in scintillator applications.

Acknowledgments

The authors thank the financial support by the National Science Foundation under CHE (award #1710160) and DMR (grant #1523577) and the USDA National Institute of Food and Agriculture (award #2015-38422-24059, for the Integrating Food Science/Engineering and Education Network (IFSEEN) program). The Department of Chemistry at the University of Texas Rio Grande Valley is grateful for the generous support provided by a Departmental Grant from the Robert A. Welch Foundation (Grant No. BX-0048). SKG would like to thanks United

States-India Education Foundation (USIEF) and Institute of International Education (IIE) for his Fulbright Nehru Postdoctoral Fellowship (Award# 2268/FNPDR/2017).

References:

1. M. Shang, S. Liang, N. Qu, H. Lian and J. Lin, *Chemistry of Materials*, 2017, **29**, 1813-1829.
2. S. Li, D. Tang, Z. Tian, X. Liu, T. Takeda, N. Hirosaki, F. Xu, Z. Huang and R.-J. Xie, *Journal of Materials Chemistry C*, 2017, **5**, 1042-1051.
3. J. Xu, D. Murata, J. Ueda and S. Tanabe, *Journal of Materials Chemistry C*, 2016, **4**, 11096-11103.
4. V. Havasi, B. Vödrédi and Á. Kukovecz, *Catalysis Today*, 2017, **284**, 107-113.
5. C. W. Kim, T. Y. Eom, I. S. Yang, B. S. Kim, W. I. Lee, Y. S. Kang and Y. S. Kang, *Scientific reports*, 2017, **7**, 6849.
6. G. F. Knoll, *Radiation detection and measurement*, John Wiley & Sons, 2010.
7. A. Kamkaew, F. Chen, Y. Zhan, R. L. Majewski and W. Cai, *Acs Nano*, 2016, **10**, 3918-3935.
8. M. D. Birowosuto, D. Cortecchia, W. Drozdowski, K. Brylew, W. Lachmanski, A. Bruno and C. Soci, *Scientific reports*, 2016, **6**, 37254.
9. Y. Tsubota, J. H. Kaneko, M. Higuchi, S. Nishiyama and H. Ishibashi, *Applied Physics Express*, 2015, **8**, 062602.
10. P. Lecoq, *Nuclear Instruments and Methods in Physics Research Section A: Accelerators, Spectrometers, Detectors and Associated Equipment*, 2016, **809**, 130-139.
11. G. Rooh, A. Khan, H. Kim, H. Park and S. Kim, *Optical Materials*, 2017, **73**, 523-526.
12. F. Zhong, J. Zhao, L. Shi, Y. Xiao, G. Cai, Y. Zheng and J. Long, *Scientific Reports*, 2017, **7**, 4684.
13. S. Mahade, N. Curry, S. Björklund, N. Markocsan, P. Nylén and R. Vaßen, *Surface and Coatings Technology*, 2017, **318**, 208-216.
14. M. Sun and B. Huang, *Inorganic chemistry*, 2017, **56**, 7975-7984.
15. M. T. Malachevsky, D. Rodríguez Salvador, S. Leiva and C. A. D'Ovidio, *Journal of Ceramics*, 2015, **2015**.
16. X. Shu, X. Lu, L. Fan, R. Yang, Y. Ding, S. Pan, P. Zhou and Y. Wu, *Journal of materials science*, 2016, **51**, 5281-5289.
17. Y. Ji, D. Jiang, T. Fen and J. Shi, *Materials research bulletin*, 2005, **40**, 553-559.
18. J. Trojan-Piegza, S. Gierlotka, E. Zych and W. Lojkowski, *Journal of the American Ceramic Society*, 2014, **97**, 1595-1601.
19. K. Wahid, M. Pokhrel and Y. Mao, *Journal of Solid State Chemistry*, 2017, **245**, 89-97.
20. R. A. Hansel, S. Desai, S. W. Allison, A. Heyes and D. G. Walker, *Journal of Applied Physics*, 2010, 107, 016101.
21. M. Pokhrel, K. Wahid and Y. Mao, *The Journal of Physical Chemistry C*, 2016, **120**, 14828-14839.
22. A. Srivastava, *Journal of Luminescence*, 2016, **169**, 445-449.

23. S. L. Cates, E. L. Cates, M. Cho and J.-H. Kim, *Environmental science & technology*, 2014, **48**, 2290-2297.
24. Y. Eagleman, M. Weber, A. Chaudhry and S. Derenzo, *Journal of Luminescence*, 2012, **132**, 2889-2896.
25. Y. Ji, D. Jiang and J. Shi, *Journal of materials research*, 2005, **20**, 567-570.
26. J. Trojan-Piegza, E. Zych and M. Kosińska, *Radiation Measurements*, 2010, **45**, 432-434.
27. F. N. Sayed, V. Grover, K. Bhattacharyya, D. Jain, A. Arya, C. Pillai and A. Tyagi, *Inorganic chemistry*, 2011, **50**, 2354-2365.
28. M. Glerup, O. F. Nielsen and F. W. Poulsen, *Journal of Solid State Chemistry*, 2001, **160**, 25-32.
29. M. Li, D. Zhou, C. P. Li and Z. Zhao, *Materials Science in Semiconductor Processing*, 2016, **44**, 101-107.
30. I. E. Seferis and E. Zych, *Journal of Luminescence*, 2016, **169**, 838-843.
31. Y. Mao, X. Guo, J. Y. Huang, K. L. Wang and J. P. Chang, *The Journal of Physical Chemistry C*, 2009, **113**, 1204-1208.
32. Y. Mao, T. J. Park, F. Zhang, H. Zhou and S. S. Wong, *Small*, 2007, **3**, 1122-1139.
33. E. Gilardi, E. Fabbri, L. Bi, J. L. Rupp, T. Lippert, D. Pergolesi and E. Traversa, *The Journal of Physical Chemistry C*, 2017, **121**, 9739-9747.
34. T. M. H. Nguyen, L. J. Sandilands, C. Sohn, C. Kim, A. L. Wysocki, I.-S. Yang, S. Moon, J.-H. Ko, J. Yamaura and Z. Hiroi, *Nature communications*, 2017, **8**, 251.
35. K. M. Turner, D. R. Rittman, R. A. Heymach, C. L. Tracy, M. L. Turner, A. F. Fuentes, W. L. Mao and R. C. Ewing, *Journal of Physics: Condensed Matter*, 2017, **29**, 255401.
36. N. Garg, K. Pandey, C. Murli, K. Shanavas, B. P. Mandal, A. Tyagi and S. M. Sharma, *Physical Review B*, 2008, **77**, 214105.
37. P. E. Blanchard, S. Liu, B. J. Kennedy, C. D. Ling, M. Avdeev, J. B. Aitken, B. C. Cowie and A. Tadich, *The Journal of Physical Chemistry C*, 2013, **117**, 2266-2273.
38. S. Mahesh, P. P. Rao, M. Thomas, T. L. Francis and P. Koshy, *Inorganic chemistry*, 2013, **52**, 13304-13313.
39. Z. Wang, H. Zhu, L. Ai, X. Liu, M. Lv, L. Wang, Z. Ma and Z. Zhang, *Journal of colloid and interface science*, 2016, **478**, 209-216.
40. D. A. Pawlak, M. Ito, M. Oku, K. Shimamura and T. Fukuda, *The Journal of Physical Chemistry B*, 2002, **106**, 504-507.
41. M. Sunding, K. Hadidi, S. Diplas, O. Løvvik, T. Norby and A. Gunnæs, *Journal of Electron Spectroscopy and Related Phenomena*, 2011, **184**, 399-409.
42. Q.-H. Wu, M. Liu and W. Jaegermann, *Materials Letters*, 2005, **59**, 1980-1983.
43. T.-M. Pan, F.-H. Chen and Y.-H. Shao, *RSC Advances*, 2015, **5**, 51286-51289.
44. S. Rudenja, A. Minko and D. Buchanan, *Applied Surface Science*, 2010, **257**, 17-21.
45. H. Xie, Q. Liu, Y. Li, H. Lv, M. Wang, X. Liu, H. Sun, X. Yang, S. Long and S. Liu, *Semiconductor Science and Technology*, 2012, **27**, 125008.
46. K. Bomben, J. Moulder, P. Sobol and W. Stickle, *Physical Electronics, Eden Prairie, MN*, 1995.
47. M. Pokhrel, M. Alcoutlabi and Y. Mao, *Journal of Alloys and Compounds*, 2017, **693**, 719-729.
48. A. A. Kaminskii, *Laser crystals: their physics and properties*, Springer, 2013.
49. S. N. Ogugua, H. C. Swart and O. M. Ntwaeaborwa, *Sensors and Actuators B: Chemical*, 2017, **250**, 285-299.

50. H. Hoefdraad and G. Blasse, *physica status solidi (a)*, 1975, **29**.
51. C. D. M. Donega, A. Meijerink and G. Blasse, *Journal of Physics and Chemistry of Solids*, 1995, **56**, 673-685.
52. G. Aumüller, W. Köstler, B. Grabmaier and R. Frey, *Journal of Physics and Chemistry of Solids*, 1994, **55**, 767-772.
53. P. Boutinaud, E. Pinel, M. Oubaha, R. Mahiou, E. Cavalli and M. Bettinelli, *Optical Materials*, 2006, **28**, 9-13.
54. K. Jaroszewski, M. Chrunik, P. Głuchowski, E. Coy, B. Maciejewska, R. Jastrzab, A. Majchrowski and D. Kasprowicz, *Optical Materials*, 2016, **62**, 72-79.
55. L. Noto, M. Chithambo, O. Ntwaeaborwa and H. Swart, *Journal of Alloys and Compounds*, 2014, **589**, 88-93.
56. Y. Guan, T. Tsuboi, Y. Huang and W. Huang, *Dalton Transactions*, 2014, **43**, 3698-3703.
57. F. Chun, B. Zhang, H. Su, H. Osman, W. Deng, W. Deng, H. Zhang, X. Zhao and W. Yang, *Journal of Luminescence*, 2017, **190**, 69-75.
58. H. Dornauf and J. Heber, *Journal of Luminescence*, 1980, **22**, 1-16.
59. B. Liu, J. Shi, Q. Wang, H. Tang, J. Liu, H. Zhao, D. Li, J. Liu, X. Xu and Z. Wang, *Journal of Luminescence*, 2018, **196**, 76-80.
60. S. K. Gupta, P. Ghosh, N. Pathak, A. Arya and V. Natarajan, *RSC Advances*, 2014, **4**, 29202-29215.
61. S. K. Gupta, P. S. Ghosh, A. K. Yadav, S. N. Jha, D. Bhattacharyya and R. M. Kadam, *Inorganic chemistry*, 2016, **56**, 167-178.
62. S. K. Gupta, P. S. Ghosh, A. K. Yadav, N. Pathak, A. Arya, S. N. Jha, D. Bhattacharyya and R. M. Kadam, *Inorganic chemistry*, 2016, **55**, 1728-1740.
63. S. K. Gupta, S. Nigam, A. K. Yadav, M. Mohapatra, S. N. Jha, C. Majumder and D. Bhattacharyya, *New Journal of Chemistry*, 2015, **39**, 6531-6539.
64. S. K. Gupta, M. Sahu, K. Krishnan, M. Saxena, V. Natarajan and S. Godbole, *Journal of Materials Chemistry C*, 2013, **1**, 7054-7063.
65. N. Li, H. Xiao, X. T. Zu, L. M. Wang, R. C. Ewing, J. Lian and F. Gao, *Journal of Applied Physics*, 2007, **102**, 063704.
66. A. Dobrowolska and E. Zych, *Journal of Luminescence*, 2017, **192**, 397-403.
67. G. H. Wannier, *Physical Review*, 1937, **52**, 191.
68. D. Liu, K. Tse and J. Robertson, *Applied physics letters*, 2007, **90**, 062901.

Table of Content: